Research Article
Vol. 34, No. 12 / 15 Jun 2026 / Optics Express 21563
Optics EXPRESS

High-speed computational imaging achieved by fly-scan ptychography

AUGUSTAS KARPAVICIUS,[1,2,3,*] MATTHIAS GOUDER,[1,2] AND STEFAN WITTE[1,2,3]

[1] *Advanced Research Center for Nanolithography, Science Park 106, 1098 XG Amsterdam, The Netherlands*
[2] *LaserLaB, Vrije Universiteit Amsterdam, De Boelelaan 1081, 1081 HV Amsterdam, The Netherlands*
[3] *Imaging Physics, Faculty of Applied Sciences, Technische Universiteit Delft, Building 22, Lorentzweg 1, 2628 CJ Delft, The Netherlands*
[*] *akarpavicius@tudelft.nl*

Abstract: Ptychography is a widely used computational imaging technique capable of reconstructing both the complex object and the illumination field. However, as a scanning-based imaging method, its acquisition speed is inherently limited, and in high-flux regimes, the total measurement time is often dominated by sample positioning and settling overhead rather than exposure time. To overcome this limitation, fly-scan ptychography was introduced, in which the sample is translated continuously during each exposure. This approach maximizes acquisition duty cycle but introduces motion-induced blurring of the diffraction patterns, which is typically addressed using probe-mode or object-mode decomposition. In existing implementations, these methods require precise synchronization between sample motion and detector acquisition, relying on accurate knowledge of the fly-scan trajectory. In this work, we introduce a modified ptychographic forward model that leverages automatic differentiation to simultaneously reconstruct not only the object and probe, but also the fly-scan trajectory directly from the measured data, without requiring precise synchronization or prior knowledge of the sample path. We demonstrate, through both numerical simulations and experimental measurements, accurate fly-scan path retrieval for extended scan lengths, achieving diffraction-limited resolution. We show that trajectory retrieval significantly improves reconstruction quality compared to approaches based on spline-interpolated scan paths. By directly comparing retrieved fly-scan trajectories with independently measured ground-truth paths, we confirm good agreement. This approach eliminates the need for high-speed position tracking and tight hardware synchronization, reducing experimental complexity and cost, and enabling fly-scan operation to be readily implemented in conventional step-scan ptychography setups.

1. Introduction

Ptychography is a computational imaging technique that has found applications across a wide range of fields, not only enabling the reconstruction of complex objects, achieving record spatial resolutions [1–3], extending to three-dimensional imaging [4–7], but also recovering complex illuminations from the infrared/visible [8–10] to the X-ray regime [11–13]. In current experimental ptychographic setups with sufficiently long exposure times (hundreds of milliseconds), the effective data acquisition time constitutes approximately half of the total measurement duration, with the remaining time dominated by overhead associated with sample repositioning. As the flux of modern lasers, X-ray sources and synchrotrons continues to increase, exposure times are expected to decrease significantly [14]. Consequently, the proportion of time lost to sample motion will grow, making sample positioning the primary bottleneck in overall measurement time. Implementing continuous exposure during sample motion in a fly-scan

#597690
https://doi.org/10.1364/OE.597690
Journal © 2026
Received 19 Mar 2026; revised 11 May 2026; accepted 12 May 2026; published 4 Jun 2026

Optics EXPRESS

measurement setup effectively mitigates this inefficiency by maximizing the duty cycle of data collection [15].

However, the continuous motion of the sample during each exposure introduces a form of spatial averaging that can be interpreted as a decoherence effect [16]. This motion-induced blur reduces the contrast of high-frequency features in the recorded diffraction patterns, ultimately compromising the fidelity and resolution of the reconstructed image [4,17,18]. A common early strategy to address the motion-induced blurring of diffraction patterns in fly-scan acquisition is probe-mode decomposition [14,15,18,19]. This method models the movement of the object as a superposition of multiple incoherent probe modes. However, it is inherently limited to linear scan trajectories, which still involve overhead at the ends of each line as the stage needs to change direction abruptly. Additionally, it assumes far-field conditions, where the assumption that shifts in the sample are equivalent to shifts in the probe breaks down in near-field regimes. The need to reconstruct multiple probe modes also increases computational cost and reduces the strength of the reconstruction constraints. To overcome these limitations, the object-mode decomposition approach was introduced [20]. By modeling the object as a sum of identical modes shifted along the fly-scan trajectory, this method enables reconstruction from arbitrary scan paths, reduces computational cost by using a single probe mode, and remains valid in near-field conditions. However, this approach relies on precise knowledge of the sample trajectory during each exposure, requiring high-speed and high-precision readout of the sample position, typically through fast interferometric tracking [17], which may be technically demanding or cost-prohibitive.

In this work, we address the blurring in fly-scan datasets by modifying the forward model to incorporate object-mode decomposition, while simultaneously leveraging automatic differentiation to reconstruct the actual scan trajectory followed by the sample. Automatic differentiation enables embedding the fly-scan trajectory reconstruction directly into the forward model. In contrast, analytical approaches struggle to invert such coupled, nonlinear problems and therefore often rely on sequential reconstruction and trajectory optimization steps through heuristic search procedures [21]. This joint optimization eliminates the need for high-speed position tracking hardware, which is required in analytical approaches. We thus propose an automatic differentiation-based ptychographic reconstruction framework that simultaneously retrieves the object and the exposed fly-scan grid. We demonstrate the proposed method on both simulated and experimental datasets, showcasing accurate recovery of the fly-scan trajectory and improved reconstruction quality compared with cases where the true path is unknown and only an approximate spline trajectory is assumed. Finally, we quantify the gain in imaging throughput relative to conventional step-scan measurements, and in both cases achieve diffraction-limited reconstructions enabled by the automatic-differentiation-based object-mode decomposition framework.

2. Methods

2.1. Modified ptychographic forward model

In conventional single-wavelength step-scan ptychography, the forward model for computing the estimated intensity at the detector can be described by a single equation that links the object and probe in the sample plane to the resulting diffraction pattern in the detector plane:

$$I_n^{\mathrm{est}}(\vec{k}) = \left|\mathcal{P}\left\{P(\vec{r})\cdot O(\vec{r}-\vec{R}_n)\right\}\right|^2 \tag{1}$$

where $\vec{r}$ are spatial coordinates in the sample plane, $\vec{k}$ coordinates in the detector space, $P(\vec{r})$ is the complex probe function, $O(\vec{r}-\vec{R}_n)$ object patch at a certain scanning position $\vec{R}_n$, and $\mathcal{P}$ represents the free-space propagation operator. Here, in the Born approximation [22], the interaction between the object and the probe is modeled as a simple multiplication, and the resulting exit wave is propagated to the detector via $\mathcal{P}$ to yield a diffraction pattern arising from

Optics EXPRESS

coherent interference. This process, together with aforementioned variables, is depicted in a ptychographic experimental setup in Fig. 1. In contrast, during fly-scan acquisition, where the sample is translated continuously during the exposure time T, the object position $\vec{R}_j$ becomes a time-dependent function $\vec{R}_j(t)$. The forward model must then account for the temporal integration of the resulting diffraction intensities over the exposure window, yielding:

$$I_n^{\text{est}}(\vec{k}) = \int_{t_n}^{t_n+T} \left| \mathcal{P}\left\{ P(\vec{r}) \cdot O(\vec{r} - \vec{R_n}(t)) \right\} \right|^2 dt \tag{2}$$

The continuous integration in the fly-scan forward model can be approximated by an incoherent sum over a discrete set of propagated intensities, obtained by discretizing the exposure into sufficiently small time intervals such that the object displacement within each interval does not exceed one object pixel [20]:

$$I_n^{\text{est}}(\vec{k}) = \sum_{m=0}^{N} \left| \mathcal{P}\left\{ P(\vec{r}) \cdot O(\vec{r} - \vec{R}_n(mT/N)) \right\} \right|^2 \tag{3}$$

where N denotes the number of sub-exposures sampled within the total acquisition time of a single camera exposure. In the far-field regime, the condition that object shifts remain smaller than the pixel size arises from the fact that sub-pixel object translations in the sample plane lead to changes in the intensity diffraction pattern (i.e., speckle shifts) that lie outside the spatial frequency support of the detector, effectively rendering such shifts unobservable. Equation (3) can thus be interpreted as a sum over multiple object positions, shifted in object pixel steps, for a single exposure, each contributing incoherently to the final recorded intensity. This model motivates the introduction of a shift operator S_n^m that decomposes the object into identical object modes and shifts them along the fly-scan path:

$$I_n^{\text{est}}(\vec{k}) = \sum_{m=0}^{N} \left| \mathcal{P}\left\{ P(\vec{r}) \cdot S_n^m \left\{ O(\vec{r}) \right\} \right\} \right|^2 \tag{4}$$

These object modes exist only within the propagation step - between the sample plane where each shifted mode is illuminated and the detector plane where we have a final incoherent summation into a single diffraction pattern. We implement subpixel shifts efficiently by applying a linear phase ramp in the spatial frequency domain, which corresponds to a spatial translation of the object in the sample plane. Specifically, the phase ramp is defined by a spatial frequency slope vector $\vec{\delta}_n^m$ containing two scalar components that describe the shift along the x- and y-axes for each object mode. The action of the shift operator S can thus be expressed as:

$$\mathcal{S}_n^m\{O(\vec{r})\} = \mathcal{F}^{-1}\left\{ \mathcal{F}\{O(\vec{r})\} \cdot \exp\left(2\pi i \vec{k} \cdot \vec{\delta}_n^m\right) \right\} \tag{5}$$

The shift operator defined in Eq. (5) implements real-space translations efficiently through the Fourier shift theorem. This formulation is both computationally efficient and fully differentiable, requiring only two scalar parameters per displacement. Since the entire forward model, including the shift operator, is composed of basic mathematical differentiable operations, automatic differentiation can be used to compute the gradients of the model output with respect to all independent variables (the probe, object, and scan trajectory parameters). Gradients are propagated through the computational graph using the chain rule, without the need for explicit derivation of an analytical backward model [23].

The reconstruction of the independent variables is achieved via iterative optimization of a loss (cost) function that quantifies the mismatch between the measured and estimated diffraction

Research Article | Vol. 34, No. 12 / 15 Jun 2026 / Optics Express 21566
Optics EXPRESS

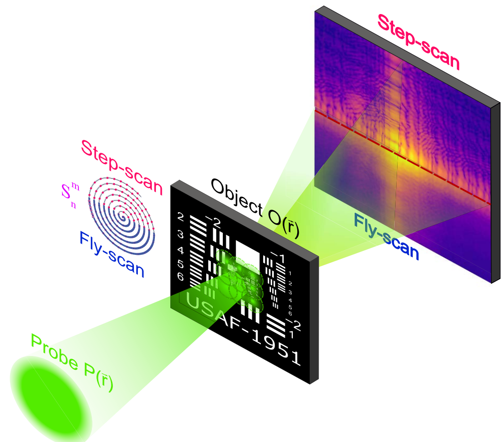

Fig. 1. Conceptual representation of ptychography: from step-scan to fly-scan. The sample plane illustrates the conceptual difference between step-scan and fly-scan sample motion, together with the shift operator S_n^m, which generates the corresponding object modes (shown in violet). These two measurement geometries lead to distinct diffraction patterns: a sharp, high-contrast pattern for the step-scan case (top) and a blurred pattern for the fly-scan case (bottom).

intensities:

$$L_n = \sum_k^K \left(\sqrt{I_n^{\text{meas}}(\vec{k})} - \sqrt{I_n^{\text{est}}(\vec{k})} \right)^2 \tag{6}$$

This amplitude-based loss function measures the squared difference between the square roots of the measured and estimated intensities, summed over all detector pixels K. Its choice is motivated by the fact that photon detection is subject to Poissonian noise even under perfect imaging conditions. In addition, the square-root transformation stabilizes the variance of Poisson-distributed measurements [24], thereby reducing the disproportionate influence of high-intensity pixels and promoting a more balanced contribution of low- and high-count regions during optimization. Alternative loss functions can also be employed, such as the negative log-likelihood [20], which is optimal under Poisson statistics, or the maximum-likelihood formulation suitable for mixed Poisson–Gaussian noise [25]. To account for non-zero detector readout noise, we also reconstruct a background intensity term representing the camera's readout signal. This term is introduced as an additional independent 2D variable that is constant over the scan positions but specific to a given camera exposure time and ambient conditions. The modified loss function then becomes:

$$L_n = \sum_k^K \left(\sqrt{I_n^{\text{meas}}(\vec{k})} - \sqrt{I_n^{\text{est}}(\vec{k}) + I^{\text{back}}(\vec{k})} \right)^2 \tag{7}$$

where $I^{\text{back}}(\vec{k})$ accounts for position-independent background contributions such as electronic readout noise and dark current. Once the loss function is defined, automatic differentiation computes its gradients with respect to all reconstruction parameters, enabling gradient-based optimization without the need for an explicitly derived inverse model.

The combination of object-mode decomposition and automatic differentiation within our independently developed AD reconstruction framework enables reconstruction of fly-scan imaged objects without prior knowledge of the precise scan trajectory. Within this framework, object-mode decomposition permits modeling arbitrary, non-periodic sample motion paths [20] and accommodates both near-field and far-field imaging geometries. While automatic differentiation

Optics EXPRESS

provides a direct and differentiable means to recover the actual fly-scan exposure path from the measured data - an otherwise analytically intractable problem that would typically require heuristic [21] or hardware-based [17] tracking approaches. This novel capability relaxes the need for tight synchronization between sample motion and detector acquisition, reducing dependence on complex interferometric tracking systems commonly used for high-speed scanning. Consequently, the proposed framework simplifies experimental implementation, facilitating the integration of fly-scan operation into existing step-scan setups across a wide range of conventional imaging geometries, including reflection-based configurations. Furthermore, the differentiable forward model demonstrates increased robustness against sample stage jitter, mechanical vibrations, and encoder latency, as these effects can be implicitly compensated through trajectory reconstruction during optimization.

2.2. Methods and simulations

To evaluate the proposed method, we simulated an experimentally realistic fly-scan ptychographic measurement of a USAF resolution target. The detector was modeled with an effective pixel size of 7.38 µm (to simulate 2×2 binning) and 1352 pixels along each axis, corresponding to an active area of approximately 10x10 mm, positioned 4.9 cm downstream from the sample. As the illumination we used a 532 nm coherent beam of 10^8 photon flux, modeled as a Gaussian probe with a 400 µm diameter, yielding an oversampling ratio [26] of 85. Diffraction pattern blurring characteristic for fly-scan acquisition was simulated by incoherently summing 15 diffraction patterns separated by approximately one object pixel (~2.5 µm), corresponding to a total fly distance of ~37.5 µm. Noise characteristics were chosen to match those of our visible experimental setup (see next section). Each diffraction pattern was modulated by 0.5% peak-to-peak laser power noise, Poisson noise was applied to reflect the discrete photon statistics, and photon number to counts were converted according to the camera quantum efficiency and pixel well depth. Gaussian readout noise (mean μ = 158 counts, standard deviation σ = 5.4 counts) was added after incoherent summation, reproducing the read-out noise observed experimentally with our detector. As a result, even the step-scan reconstruction exhibits slight imperfections, as seen in Fig. 2 (column "Step-scan"). The simulation used 100 scanning positions with a 38 µm step size, corresponding to a 91% geometric overlap. Reconstruction quality was quantified using the complex correlation coefficient [27]. For the step-scan case, we obtain C = 0.97 and successfully resolve the second element of the first group (4 µm line separation), consistent with a near diffraction-limited reconstruction for a 2.5 µm object pixel size. This reconstruction serves as the reference for the fly-scan comparisons.

When a fly-scan measurement is reconstructed with a conventional forward model (no object mode-decomposition), significant blurring appears in the recovered object, reflected by a reduced complex correlation coefficient of C = 0.86 as can be seen in Fig. 2 "Without decomposition" column. The original fly-scan trajectory is shown in blue, while the averaged scan grid, corresponding to an exposure integrated over the distance of 15 object pixels, is shown in red. Lacking prior knowledge of the true trajectory, we decomposed each averaged position into 15 object modes (based on the fly-scan distance and object pixel size) and placed these modes on a spline-approximated grid generated by fitting a cubic spline to the averaged coordinates. It is important to note that this spline-based initialization represents a constrained scenario in which only a single averaged position per detector exposure is available, without access to high-frequency position measurements or explicit exposure-window information. The denser spline grid is therefore obtained solely by interpolating these averaged positions to initialize the 15 object modes. This spline-based object-mode decomposition yields visibly improved reconstruction quality and a higher complex correlation coefficient. However, the spline grid deviates from the true fly-scan path, most notably near the center, where the trajectory exhibits

Optics EXPRESS

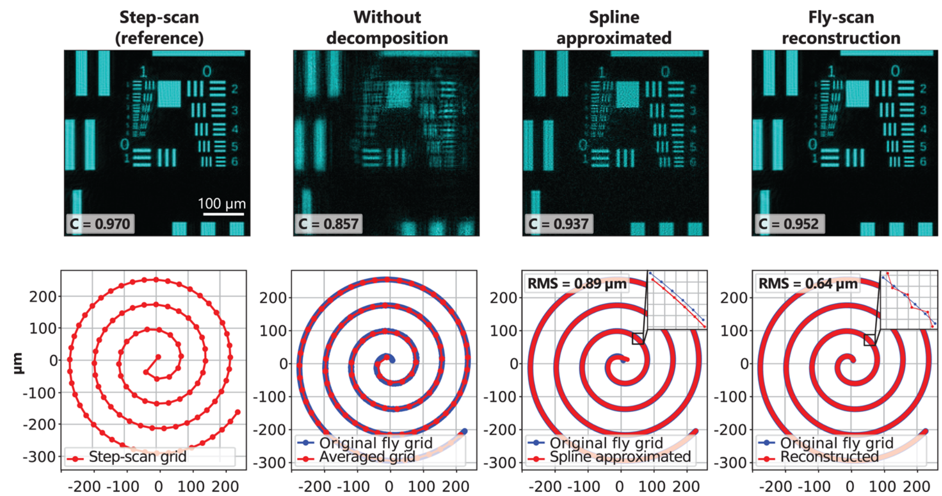

Fig. 2. Simulation results. Reconstructed objects and their corresponding complex correlation coefficients C shown alongside the scan grids used in each case. The first column presents the step-scan reference reconstruction. The remaining columns correspond to fly-scan measurements reconstructed using three different strategies: (i) conventional reconstruction without object-mode decomposition, (ii) object-mode decomposition using a spline-approximated scan grid, and (iii) object-mode decomposition combined with fly-scan path retrieval within the forward model. In the scan-grid plots, the blue trajectory represents the true fly-scan path used in the simulation of the diffraction patterns, while the red trajectory denotes the scan grid used during reconstruction. The reported RMS value indicates the root-mean-square deviation between these two trajectories.

a small radius of curvature. However, as can be seen from the inset of the Fig. 2 "Spline-approximated" column, the spline approximation underestimates the curvature of the outer arcs as well. These discrepancies are quantified using the root-mean-square (RMS) distance between the original and spline-approximated grids. Finally, with the modified forward model including automatic differentiation enabled retrieval of the object mode shifts during reconstruction, the recovered object closely matches the step-scan reference, and the reconstruction approaches near diffraction-limited resolution. An important practical detail is that all AD-based fly-scan trajectory reconstructions are initialized using the spline-approximated fly-scan grid as the initial position estimate. This provides a physically reasonable starting point for the trajectory optimization, which is subsequently refined during reconstruction. The reconstructed fly-scan grid shows reduced deviations from the original fly-scan path, with all discrepancies falling within one object pixel distance. At this scale, many residual shifts produce intensity variations outside the recorded detector area and therefore do not contribute significantly to the loss. Within these limits, the method successfully recovers the fly-scan trajectory and delivers a visible improvement in reconstruction quality compared to the spline-approximated reconstructions.

3. Experimental results

3.1. Experimental setup for fly-scan ptychography

Although the primary goal of this work is to demonstrate that fly-scan ptychography can be performed without precise synchronization or high-accuracy sample motion control, a fully synchronized measurement setup was implemented to validate the reconstructed fly-scan trajectory. The setup is depicted in Fig. 3, in which the sample motion, position tracking, and camera exposure are all synchronized to the laser pulse train. The mode-locked output of a home-built

Research Article Vol. 34, No. 12 / 15 Jun 2026 / *Optics Express* 21569
Optics EXPRESS

Nd:YVO_4 laser serves as the master timing reference for the digital delay generator (Stanford Research Systems DG645). The delay generator down-samples the laser clock and distributes two synchronized timing signals: one to the waveform generator (National Instruments PCIe-6321), which in turn drives the sample stage controller, and another to the camera (Allied Vision Prosilica GT 3400), which triggers its exposure.

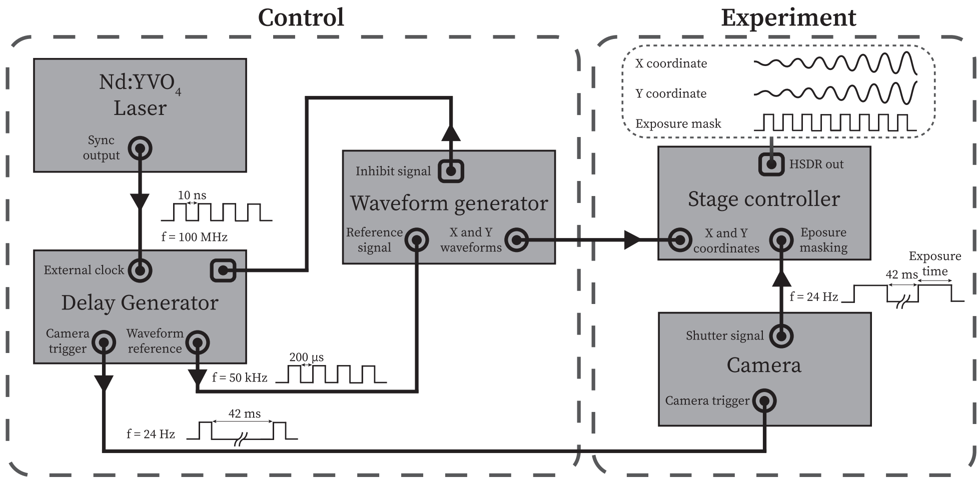

Fig. 3. Conceptual diagram of the experimental setup synchronization scheme. The schematic illustrates how illumination, sample motion, camera exposure, and position tracking are synchronized, enabling accurate correlation of diffraction patterns with the exposed regions of the fly-scan grid.

The measurement sequence is initiated by a user command that first prepares the waveform generator to wait for an external clock signal. Once prepared, an uninhibit signal is sent to the delay generator, enabling it to output the synchronized timing pulses which are used to reference the analog output. The waveform generator then outputs analog signals corresponding to the x- and y-coordinates of the sample trajectory, while the camera trigger defines the exposure timing. The exposure length is set on the camera before the experiment, which in combination with the camera trigger, makes up the shutter signal. These signals are received by the sample stage controller (SmarAct MCS2-C-0021), which thus obtains three analog inputs: two for sample positioning (x,y) and one shutter signal indicating the exposure masking. The controller drives a two-dimensional sample stage composed of two SmarAct SLC-1760 linear piezo stages and operates in the "External Sensor Correction via Analog Input" mode, where the incoming voltage signals are interpreted as continuously updated position offsets relative to the initial stage position. Moreover, the stage controller continuously records the actual sample position at a 50 kHz sampling rate, allowing precise retrieval of the sample trajectory. The resulting fly scan grid, consisting of synchronized time-stamped x- and y-coordinates together with the exposure mask, is shown in Fig. 3 above the controller. This configuration ensures an exact temporal correspondence between the recorded diffraction frames and the sample positions, enabling high-precision validation of the reconstructed fly-scan path. While we used a pulsed laser because it was readily available, we emphasize that similar performance can also be achieved using a sufficiently bright continuous-wave laser and a suitable timing reference (which may be the delay generator itself), which would reduce the overall equipment cost.

Optics EXPRESS

3.2. Experimental reconstruction with an unknown fly-scan path

Using the experimental setup described above, we performed step-scan and fly-scan ptychographic measurements to evaluate the proposed modified fly-scan forward-model reconstruction framework on real data. The scans followed an equidistant Archimedean spiral trajectory covering a 0.99 mm^2 field of view with 158 scan positions in the step-scan mode. A structured probe was used with an average power of 1 µW and an effective mode diameter of 404 µm, resulting in a geometrical overlap of 84% and an oversampling ratio of 43. The measurement geometry matched that used in the simulations, with a sample-detector distance of 4.87 cm and a detector active area of 10x10 mm, composed of 3.69 µm pixels (2×2 binned), corresponding to a numerical aperture of 0.1 and an object pixel size of 2.5 µm. During fly-scan acquisition, the stage velocity was chosen such that the sample traversed approximately 15 object pixels (36.4 µm) per exposure of 20 ms. Two samples with two different fly-scan grids were measured: a highly scattering USAF resolution target (first row of Fig. 4) and a weakly scattering biological testicular tissue slice (second row). The step-scan reconstruction achieves diffraction-limited reconstruction, resolving the third element of the seventh group of the USAF target (highlighted in red), corresponding to a line width of 3.1 µm. For fly-scan measurements, trends consistent with the performed simulations are observed. Reconstructions using the conventional forward model without mode decomposition exhibit severe motion-induced blurring. Introducing object-mode decomposition on a spline-approximated scan grid leads to a moderate improvement in reconstruction sharpness. However, the residual mismatch between the spline grid and the true fly-scan trajectory introduces pronounced high-frequency amplitude noise in both the USAF target and the biological sample. This results in reduced image sharpness, with fine structural details lost in the spline-approximated reconstruction. As shown in the zoomed insets of Fig. 4, the third element of the USAF target is no longer resolved, and the cell wall in the biological sample cannot be clearly distinguished in some locations. In contrast, the proposed forward model incorporating simultaneous fly-scan path retrieval achieves reconstructions for both samples that are visually comparable to the step-scan reference. The improved reconstruction quality is attributed to the accurate recovery of the fly-scan trajectory, which differs from the spline-approximated grid, as will be discussed in a later section.

To quantitatively assess the resolution improvement obtained through fly-scan path retrieval, we employed two complementary metrics: knife-edge analysis and Fourier ring correlation (FRC) [28], as shown in Fig. 5. Knife-edge analysis was performed by evaluating the 10-90% intensity rise across selected sharp edge, indicated by a dashed red line in the inset of Fig. 5(A). As the measurements approach the diffraction limit, only a few data points span the intensity rise of the edge, making direct interpolation of the 10–90% intensity levels unreliable and highly susceptible to noise. Therefore, the edge profiles were fitted with an error function, which models the convolution of a sharp edge with a Gaussian point-spread function, enabling robust estimation of the 10–90% rise width [29]. For the vertical profile, the fitted widths were 1.6 px (3.1 µm), 6.4 px (12.8 µm), and 2.0 px (4.0 µm) for the fly-scan path-retrieved, spline-approximated, and step-scan reconstructions, respectively. For the horizontal profile (not shown due to its close similarity to the vertical lineout), the corresponding widths were 1.8 px (3.6 µm), 8.3 px (16.6 µm), and 2.0 px (4.0 µm). The reconstructions were performed with an object pixel size of 2 µm, slightly below the diffraction limit of 2.5 µm, to avoid any possible resolution quantization effects when using a speckled probe. It should be emphasized that knife-edge analysis provides a local and noise-sensitive resolution estimate and is therefore used here primarily for relative comparison between reconstruction strategies. The path-retrieved reconstruction achieves edge sharpness comparable to the step-scan reference, with the intensity transition spanning only a few pixels, as can be observed when zooming in the inset of Fig. 5(A), which depicts fly-scan path-retrieved reconstruction. In contrast, the spline-approximated reconstruction exhibits significantly degraded edge quality.

Optics EXPRESS

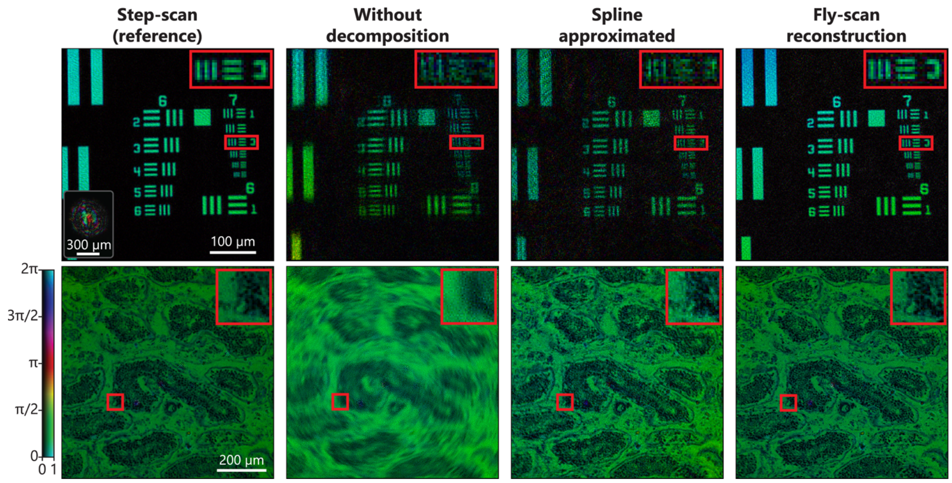

Fig. 4. Experimental step-scan and fly-scan reconstructions for a highly scattering object (USAF resolution target) and a weakly scattering object (testicular tissue slice). The first column shows the step-scan reference reconstruction for both samples. The subsequent columns display fly-scan reconstructions obtained using three different strategies, consistent with the performed simulations: (i) conventional reconstruction without object-mode decomposition, (ii) object-mode decomposition on a spline-approximated scan grid, and (iii) object-mode decomposition with simultaneous fly-scan path retrieval. Image brightness represents the normalized object amplitude (horizontal colorbar axis), while hue encodes the phase information (vertical colorbar axis).

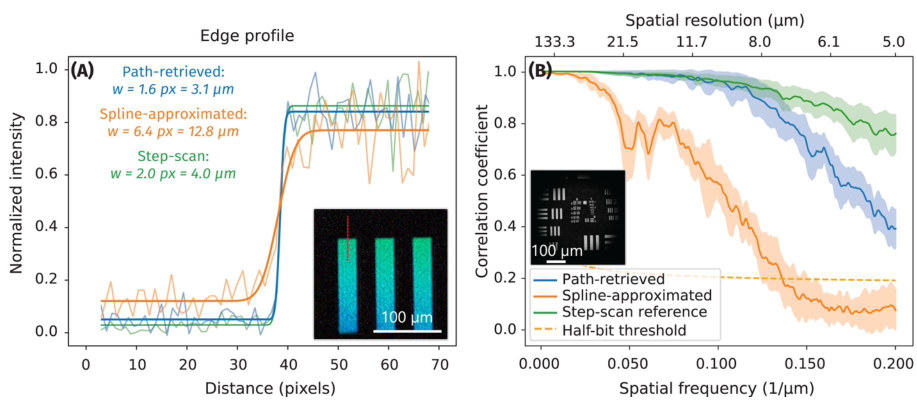

Fig. 5. Resolution assessment. (A) Knife-edge analysis of vertical intensity profiles fitted with error functions for the path-retrieved, spline-approximated, and step-scan reconstructions. The inset shows the selected vertical edge profile (dashed red line) on the path-retrieved reconstruction. (B) Fourier ring correlation (FRC) curves for the three reconstruction strategies, obtained by averaging ten independent FRC measurements; the mean curves and corresponding standard deviations are shown. The inset indicates the field of view used for the FRC analysis.

Optics EXPRESS

To obtain a global resolution estimate, we further performed Fourier ring correlation (FRC) [28,30]. FRC measures the correlation coefficient between two independently reconstructed complex object spatial spectra on concentric frequency rings of finite thickness, as the ring radius is varied. The resulting FRC curve therefore quantifies reconstruction consistency as a function of spatial frequency, where the decay at higher frequencies reflects the decreasing signal-to-noise ratio [30]. It is important to note that the final FRC data point corresponds to the full-pitch resolution, as the highest accessible spatial frequency has a two-pixel period, while the resolution values discussed above and below are reported in terms of half-pitch (one-pixel) resolution. Five independent reconstructions were performed using different initial guesses, including random 10% amplitude and phase perturbations for the initial probe guess and random amplitude initialization for the object guess. The resulting ten FRC curves were averaged to depict the mean FRC curve together with standard deviation, as shown in Fig. 5(B). Using the half-bit threshold criterion [31], both the step-scan and fly-scan path-retrieved reconstructions achieve a half-pitch resolution of 2.5 μm, confirming diffraction-limited performance. In contrast, the spline-approximated reconstruction reaches only 3.7 μm half-pitch resolution, demonstrating that fly-scan path retrieval significantly improves the achievable resolution.

3.3. Retrieved fly-scan paths

To validate whether the fly-scan path reconstructed by the modified ptychographic forward model corresponds to the true sample trajectory during the measurement, we independently recorded the sample motion using high-speed position tracking enabled by the setup described in Sec. 3.1. Figure 6 compares the experimentally measured fly-scan path (red) with the spline-approximated path (gray) and the reconstructed fly-scan path obtained from the ptychographic reconstruction (blue). Figure 6 (A) shows the fly-scan grid used for the USAF resolution target measurements presented in Fig. 4, while Fig. 6 (B) depicts a more complex flower-shaped fly-scan grid designed to challenge spline-based path approximation. The flower-shaped trajectory was scanned at a lower velocity to ensure that the sample stage could accurately follow its high-curvature small features. To maintain comparable motion blur conditions, the exposure time was increased to 30 ms, resulting in an average displacement of approximately 15 object pixels per exposure, similar to the spiral scan. This flower-shaped trajectory was also used for USAF resolution target measurements, for which diffraction-limited resolution was achieved by performing fly-scan path retrieval. In both cases, the retrieved fly-scan path exhibits good agreement with the independently measured trajectory. The modified forward model successfully reconstructs the exposure windows, correctly grouping object modes within the exposure intervals and in that way identifying camera dead-time regions during which the stage continues to move while no exposure is taking place. This is one of the main reasons for the observed improvement in reconstruction quality, observed in Fig. 4 when comparing reconstructions based on spline-approximated and retrieved fly-scan grids. In addition, Fig. 6 (B) demonstrates that the method not only recovers exposure intervals but also accurately reconstructs the geometry of a complex, highly curved fly-scan trajectory, particularly in the inner regions where spline interpolation underestimates additional curvature. The improvement in fly-scan grid accuracy is quantified by computing the RMS distance between the measured fly-scan path and both the reconstructed and spline-approximated grids. For the spiral scan, the RMS distance decreases from 9.7 μm for the spline approximation to 4.1 μm for the retrieved path. For the flower-shaped grid, the distance is reduced from 3.9 μm to 2.2 μm, which is below a single object pixel size. A relevant observation is that in Fig. 6 (A) a small number of reconstructed object modes deviate from the true scan path. These deviations arise from large separations between successive exposure intervals caused by high stage velocity, where the initial spline approximation places some object modes far from the true trajectory, leading to slow convergence or in some cases - failure to converge to the correct position. Such deviations are not observed for the flower-shaped trajectory, where the lower scan velocity results in shorter dead-time intervals and therefore a more accurate spline-based initialization, placing the object modes closer to the true trajectory prior to optimization. Importantly, such deviations occur for only a single mode out of the 15 object modes associated with each exposure, as illustrated in the right side of Fig. 6 (A). The remaining modes accurately follow the true scan path, and since all modes are incoherently summed to form a single blurred diffraction pattern, the contribution of an individual deviated mode to the total loss function is small. Consequently, these isolated deviations do not significantly affect the overall reconstruction quality.

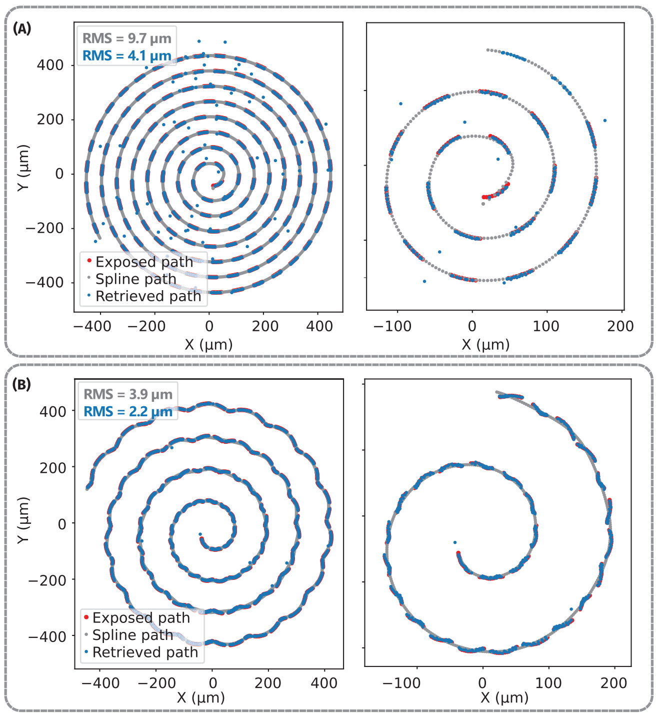

Fig. 6. Fly-scan path comparison. The measured fly-scan exposure path obtained from high-speed sample tracking (red) is compared with the fly-scan path retrieved by the modified ptychographic forward model (blue) and with the spline-interpolated path (gray). (A) Scan grid used for the USAF resolution target in Fig. 4 (left). (B) Flower-shaped fly-scan grid, used for USAF resolution target measurement (left), designed to illustrate the limitations of spline interpolation. Right sides show a zoomed central region, highlighting the decomposition of a single exposure into 15 object modes and their agreements with the measured grid.

To further evaluate the performance of the modified forward model, we performed a series of fly-scan measurements with progressively increasing fly-scan path length, ranging from 5 to 25 object modes per exposure. To ensure a fair comparison across measurements, we maintained a constant amount of information content by fixing the exposure time to 20 ms (which ensures a constant photon flux), as well as a constant total number of diffraction patterns, and identical field of view. For longer fly-scan paths, this was achieved by increasing the ring density within the same field of view, as illustrated in Fig. 7 (A). Although the consequence of this specific comparison is that the overlap varies between the scans, this does not influence the reconstruction quality, since the probe diameter of approximately 400 µm spans roughly half of the scan-grid extent, covering many neighboring positions in any scan-grid configuration. In Fig. 7 (A), the red patches indicate the exposed fly-scan trajectories, while the black dots denote the averaged scan positions that are provided as input to the reconstruction algorithm. As in previous experiments, no high-speed or high-precision knowledge of the true sample trajectory is assumed. These averaged positions are then spline-interpolated and refined during reconstruction using the modified fly-scan forward model. For each fly-scan path length, we performed four independent reconstructions, where each reconstruction was initialized with a probe estimate perturbed by 10% random amplitude and phase noise, while the object was initialized with random amplitude. During reconstruction, the probe, object, fly-scan path, and detector background were simultaneously updated. The resulting independent reconstructions were used to compute six FRC curves for each fly-scan measurement with different path lengths. Figure 7 (B) shows the mean FRC curves with standard deviations for each fly-scan length, together with insets of the reconstructed second and third element of the seventh group of the USAF resolution target (3.48 µm and 3.1µm linewidth, respectively). As expected, increasing the fly-scan path length leads to a gradual degradation in reconstruction quality. For short paths corresponding to 5 object modes per exposure, the achieved resolution is comparable to that of the step-scan reference. Diffraction-limited performance is maintained up to approximately 20 object modes for this measurement geometry. For the longest path length of 25 object modes, the resolution degrades to a half-pitch value of approximately 3 µm (6 µm full pitch). Although the third element of the USAF target remains resolvable, as shown in the inset, the reconstruction quality at the smallest spatial scales is visibly degraded. However, this degradation is not caused by reduced accuracy of the retrieved fly-scan path, since the number of deviated object modes remains approximately constant at about one mode per exposure, and the reconstructed fly-scan paths remain in close agreement with the measured trajectories. Instead, the observed resolution loss is attributed to the superposition of a high number of diffraction patterns within a single exposure, leading to stronger blurring in the recorded diffraction data, which substantially complicates the deblurring problem during reconstruction for long fly-scan paths [20].

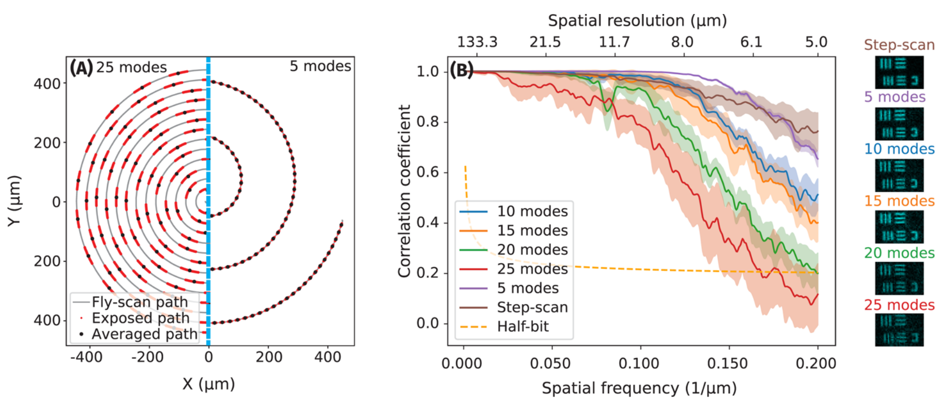

Fig. 7. Influence of fly-scan path length. (A) Fly-scan grid composition for increasing path lengths at constant field of view, illustrated for 5- and 25-mode limits. Exposed trajectories are shown in red, and the averaged scan positions used in reconstruction are indicated by black dots. (B) Mean Fourier ring correlation curves with standard deviation for reconstructions at different fly-scan path lengths, together with the second and third elements of the reconstructed USAF resolution target for each case. For the FRC analysis shown here, the same field of view was used as indicated in the inset of Fig. 5(B).

4. Discussion and conclusions

The implementation of the modified fly-scan forward model demonstrates improved reconstruction quality without requiring precise prior knowledge of the fly-scan trajectory and, therefore, without the need for a high-speed, high-precision sample tracking system. When comparing reconstructions based on spline-approximated grids to those obtained via fly-scan path retrieval, we observe a significant improvement in reconstruction fidelity together with accurate recovery of the experimentally measured trajectory. It is important to note that even for longer fly-scan paths, the reconstructed scan grid remains in good agreement with the measured trajectory. This indicates that the degradation in reconstruction quality observed for extended fly distances does not arise from failure of the fly-scan path retrieval. Rather, scanning over longer distances increases the number of object modes contributing to each exposure, making the deconvolution more challenging. At the same time, high spatial frequency intensity components become increasingly blurred, reducing their amplitude and causing them to approach the detector background level. In such cases, even correct object mode placement cannot fully recover the speckles drowning in noise, which ultimately limits the achievable reconstruction quality.

From a computational perspective, the improved experimental efficiency comes at the cost of increased reconstruction time. All reconstructions (step-scan and the different fly-scan strategies) were run for 6000 iterations. Although this number is much higher than typically needed, it was chosen to ensure comparable convergence across all strategies and different fly-scan path lengths. As the number of object modes increases, the computational cost per iteration grows approximately linearly, meaning that longer fly-scan paths require proportionally longer reconstruction times.

Experimentally, the current bottleneck in measurement speed is the CCD camera readout rate, which under our experimental conditions is limited to 24 frames per second, rather than the stage motion itself. In principle, shorter acquisition times of only a few seconds would be possible. However, this would significantly reduce the number of recorded diffraction patterns, complicating the reconstruction and convergence of the algorithm. Further reductions in acquisition time could be achieved by employing faster CMOS cameras in combination with a sufficiently bright source, in which case the stage motion would likely become the dominant limiting factor.

In the present implementation, stage positioning is not the primary limiting factor due to the use of an equidistant Archimedean spiral trajectory, which provides a continuous scan path without abrupt directional changes and therefore reduces the acceleration demands on the sample stage. This allows operation at a constant scan velocity while remaining within the motion capabilities of the hardware. Alternative scan trajectories, including random or straight-line patterns, are also compatible with the proposed framework, but may lead to longer scan times if they involve rapid changes in motion direction that require higher stage accelerations. In addition, moderate variations in scan velocity can be accommodated by varying the number of decomposed object modes for each exposure.

Overall, the proposed method enables diffraction-limited reconstructions for fly-scan distances of up to 20 object pixels. Under these conditions, the total acquisition time is reduced from 40 s for the step-scan measurement to 6.5 s for the fly-scan measurement, corresponding to more than a fivefold improvement in measurement speed. This reduction in measurement time, achieved without sacrificing reconstruction resolution, increases the space–bandwidth product per unit time [32,33] from 18.8 Mpix/s (step-scan) to 101.8 Mpix/s (fly-scan), given a half-pitch resolution of 2.5 µm and a field of view of 0.99 mm^2. Furthermore, while maintaining the same number of 158 diffraction patterns acquired with 20 ms exposure time, the fraction of wasted time [14], during which no signal is recorded, decreases from 92% in step-scan operation to 58.3% in fly-scan operation. These results demonstrate that fly-scan acquisition, combined with the modified fly-scan forward model, substantially improves measurement efficiency without increasing experimental complexity.

Funding. Dutch Research Council (19405).

Acknowledgment. We thank Jorijn Kuster for extensive support on the synchronization hardware and data acquisition software. We also thank Matthijs Velsink for his valuable consultancy regarding the experimental setup.

Disclosures. The authors declare no conflicts of interest.

Optics EXPRESS

Data availability. Data and reconstruction code will be provided by the authors upon reasonable request.

References

1. Z. Chen, Y. Jiang, Y.-T. Shao, *et al.*, "Electron ptychography achieves atomic-resolution limits set by lattice vibrations," Science **372**(6544), 826–831 (2021).
2. Y. Jiang, Z. Chen, Y. Han, *et al.*, "Electron ptychography of 2d materials to deep sub-Ångström resolution," Nature **559**(7714), 343–349 (2018).
3. H. Yang, R. Rutte, L. Jones, *et al.*, "Simultaneous atomic-resolution electron ptychography and z-contrast imaging of light and heavy elements in complex nanostructures," Nat. Commun. **7**(1), 12532 (2016).
4. T. Aidukas, N. W. Phillips, A. Diaz, *et al.*, "High-performance 4-nm-resolution X-ray tomography using burst ptychography," Nature **632**(8023), 81–88 (2024).
5. M. Dierolf, A. Menzel, P. Thibault, *et al.*, "Ptychographic X-ray computed tomography at the nanoscale," Nature **467**(7314), 436–439 (2010).
6. B. Chen, M. Guizar-Sicairos, G. Xiong, *et al.*, "Three-dimensional structure analysis and percolation properties of a barrier marine coating," Sci. Rep. **3**(1), 1177 (2013).
7. M. Holler, M. Guizar-Sicairos, E. H. Tsai, *et al.*, "High-resolution non-destructive three-dimensional imaging of integrated circuits," Nature **543**(7645), 402–406 (2017).
8. M. Du, L. Loetgering, K. S. E. Eikema, *et al.*, "Measuring laser beam quality, wavefronts, and lens aberrations using ptychography," Opt. Express **28**(4), 5022–5034 (2020).
9. G. Zheng, R. Horstmeyer, and C. Yang, "Wide-field, high-resolution Fourier ptychographic microscopy," Nat. Photonics **7**(9), 739–745 (2013).
10. M. Li, L. Bian, G. Zheng, *et al.*, "Single-pixel ptychography," Opt. Lett. **46**(7), 1624–1627 (2021).
11. C. M. Kewish, P. Thibault, M. Dierolf, *et al.*, "Ptychographic characterization of the wavefield in the focus of reflective hard X-ray optics," Ultramicroscopy **110**(4), 325–329 (2010).
12. A. Schropp, P. Boye, J. M. Feldkamp, *et al.*, "Hard X-ray nanobeam characterization by coherent diffraction microscopy," Appl. Phys. Lett. **96**(9), 091102 (2010).
13. M. Stockmar, I. Zanette, M. Dierolf, *et al.*, "X-ray near-field ptychography for optically thick specimens," Phys. Rev. Appl. **3**(1), 014005 (2015).
14. J. Deng, Y. S. Nashed, S. Chen, *et al.*, "Continuous motion scan ptychography: Characterization for increased speed in coherent X-ray imaging," Opt. Express **23**(5), 5438–5451 (2015).
15. P. M. Pelz, M. Guizar-Sicairos, P. Thibault, *et al.*, "On-the-fly scans for X-ray ptychography," Appl. Phys. Lett. **105**(25), 251101 (2014).
16. P. Thibault and A. Menzel, "Reconstructing state mixtures from diffraction measurements," Nature **494**(7435), 68–71 (2013).
17. S. Liu, Z. Xu, X. Zhang, *et al.*, "Position-guided ptychography for vibration suppression with the aid of a laser interferometer," Opt. Lasers Eng. **160**, 107297 (2023).
18. J. N. Clark, X. Huang, R. J. Harder, *et al.*, "Dynamic imaging using ptychography," Phys. Rev. Lett. **112**(11), 113901 (2014).
19. X. Huang, K. Lauer, J. N. Clark, *et al.*, "Fly-scan ptychography," Sci. Rep. **5**(1), 9074 (2015).
20. M. Odstrčil, M. Holler, and M. Guizar-Sicairos, "Arbitrary-path fly-scan ptychography," Opt. Express **26**(10), 12585–12593 (2018).
21. A. Maiden, M. Humphry, M. Sarahan, *et al.*, "An annealing algorithm to correct positioning errors in ptychography," Ultramicroscopy **120**, 64–72 (2012).
22. P. W. Hawkes and J. C. Spence, *Springer Handbook of Microscopy* (Springer, 2019).
23. S. Ghosh, Y. S. Nashed, O. Cossairt, *et al.*, "ADP: Automatic differentiation ptychography," in *International Conference on Computational Photography* (IEEE, 2018), pp. 1–10.
24. A. Rajwade and K. S. Gurumoorthy, "Two penalized estimators based on variance stabilization transforms for sparse compressive recovery with poisson measurement noise," Signal Processing **188**, 108186 (2021).
25. J. Seifert, Y. Shao, R. van Dam, *et al.*, "Maximum-likelihood estimation in ptychography in the presence of Poisson–Gaussian noise statistics," Opt. Lett. **48**(22), 6027–6030 (2023).
26. J. Miao, D. Sayre, and H. N. Chapman, "Phase retrieval from the magnitude of the Fourier transforms of nonperiodic objects," J. Opt. Soc. Am. A **15**(6), 1662–1669 (1998).
27. J. Seifert, D. Bouchet, L. Loetgering, *et al.*, "Efficient and flexible approach to ptychography using an optimization framework based on automatic differentiation," OSA Continuum **4**(1), 121–128 (2021).
28. W. O. Saxton and W. Baumeister, "The correlation averaging of a regularly arranged bacterial cell envelope protein," J. Microsc. **127**(2), 127–138 (1982).
29. B. Zhang, D. F. Gardner, M. D. Seaberg, *et al.*, "High contrast 3D imaging of surfaces near the wavelength limit using tabletop euv ptychography," Ultramicroscopy **158**, 98–104 (2015).
30. J. Vila-Comamala, A. Diaz, M. Guizar-Sicairos, *et al.*, "Characterization of high-resolution diffractive X-ray optics by ptychographic coherent diffractive imaging," Opt. Express **19**(22), 21333–21344 (2011).
31. M. van Heel and M. Schatz, "Fourier shell correlation threshold criteria," J. Struct. Biol. **151**(3), 250–262 (2005).
32. W. Eschen, C. Liu, D. S. Penagos Molina, *et al.*, "High-speed and wide-field nanoscale tabletop ptychographic EUV imaging and beam characterization with an sCMOS detector," Opt. Express **31**(9), 14212–14224 (2023).
33. A. W. Lohmann, R. G. Dorsch, D. Mendlovic, *et al.*, "Space–bandwidth product of optical signals and systems," J. Opt. Soc. Am. A **13**(3), 470–473 (1996).